Acoustic-gravity waves during solar eclipses: detection and characterization using wavelet transforms

Petra Sauli, Stéphane G. Roux, Patrice Abry, Josef Boska

Acoustic-gravity waves during solar eclipses: detection, characterization and modeling using wavelet transforms.

P. Šauli[1], S. G. Roux[2] , P. Abry[2], J. Boška[1]

(1) *Institute of Atmospheric Physics ASCR, Czech Republic, pkn@ufa.cas.cz, boska@ufa.cas.cz*
(2) *Laboratoire de Physique (UMR5672), CNRS, Ecole Normale Supérieure, Lyon, France, Patrice.Abry@ens-lyon.fr, perso.ens-lyon.fr/patrice.abry*

Abstract

In the present contribution, we first propose a methodology that enables to detect wave like structures propagating in Ionosphere, by tracking the local maxima of the modulus continuous wavelet transform coefficients through heights. From the derivation of the phases of the wavelet transform, we measure the corresponding propagating parameters. These tools are applied to measurements collected by vertical ionospheric sounding at high-time resolution sampling regime (sampling periods ranged from 1 to 3 min) in the observatory Průhonice (49.9N, 14.5E, Czech Republic). The aim of these experiments is to analyze the changes in the ionospheric plasma induced by three different solar eclipse events (total solar eclipses, 11 August 1999, 29 March 2006, and annular solar eclipse, 3 October 2005) and to detect and analyze the propagation of the generated acoustic gravity waves. Second, injecting wave vector components measured from the data into the acoustic gravity wave propagation equations, we obtain a full description of the propagation of the waves. This enables us to differentiate acoustic gravity waves from others and to discuss similarities and differences of the waves detected during these three particular events. These procedures also enabled us to detect acoustic waves. We believe that the methodology proposed here brings significant improvement in detecting, characterizing and modeling acoustic gravity wave propagations from empirical data and can be readily used in the ionosphere community.

Key words: Acoustic-Gravity Wave, Vertical Ionospheric Sounding, F-Layer, Wavelet Transform, Wave Packet Characterization

1 Introduction

Acoustic Gravity Waves in Atmosphere. Terrestrial atmosphere shows high variabilities over a broad range of periodicities, which mostly consist of wave-like perturbations characterized by various spatial and temporal scales. Amongst atmospheric waves, acoustic gravity waves (AGW), whose periodicities range from minutes (pure acoustic waves) to few hours (gravity waves), constitute the source of most of the short-time ionospheric variabilities. Acoustic gravity waves play an important role in the dynamics and energetics of Atmosphere and Ionosphere. For instance, they are responsible for momentum and energy transfers from high latitudes to low latitudes and from lower to upper Atmosphere. Because acoustic gravity waves spread energy between atmospheric regions, they significantly contribute to the global circulation, temperature and compositional structure of Mesosphere, Thermosphere and Ionosphere. Gravity waves are hence an important component of the atmospheric motion field. Acoustic gravity wave propagation also have a significant impact on radio wave propagation conditions. Therefore, analyzing and understanding wave generation mechanisms with respect to specified sources constitutes a major goal to improve our knowledge of atmospheric dynamics. Acoustic gravity wave theory (e.g. **?**) in terrestrial Atmosphere has been developed in the sixties and then further extended by various authors (e.g. **?**, **?**, **?**). The first experimental observations refer to acoustic gravity waves generated by explosive sources and earthquakes **?**, **?**, and acoustic gravity waves in Earth Atmosphere have been widely studied empirically since. The interests of scientists range from the analysis of the climatology of the gravity waves to case studies of acoustic gravity wave occurrences related to particular events acting as wave sources, such as meteorological systems, geomagnetic storm, solar eclipse etc. Various radio techniques (including ionosonde) were used around the globe to analyze the climatology and case events of acoustic gravity waves. Numerous measurements and campaigns were conducted aiming at relating the observed gravity waves to their sources (e.g. HIRAC campaign **?** amongst others). However, the description, interpretation and understanding of the mechanisms underlying acoustic gravity wave generation and propagation still remain incomplete. This is mostly due to severe difficulties in analyzing real measurements. For instance, it is difficult to decide whether the observed wave characteristics are due to the properties and positions of the acoustic gravity wave sources or to interactions between the propagating waves and the mean flow (convection, tides, planetary waves etc.), see e.g., by **?**, **?**, **?** or **?** for detailed reviews.

Acoustic Gravity Waves and Solar Eclipses. It has been proposed by **?** that solar eclipses can act as sources for acoustic gravity waves. During a solar eclipse, Ionosphere strongly reacts to the break of ionization. The lu-

nar shadow is moving within Ionospheric heights at a supersonic speed. The sharp border between sunlit and eclipsed regions, defined by strong gradients in temperature and ionization flux, moves throughout Ionosphere and drives it into a non-equilibrium state. The photoionization cut-off, together with the cooling of the neutral Atmosphere over a limited area, creates waves that tend to drive Ionosphere back to its equilibrium state. Model insights into processes occurring during solar eclipse in Thermosphere and Ionosphere is proposed by **?**. Studies by **?** suggest that perturbations generated by the eclipse induced ozone heating interruption may propagate upwards into the Thermosphere-Ionosphere system where they have an important influence. First experimental evidence of the existence of gravity waves in Ionosphere during solar eclipses were reported in **?**, where waves with periods of 30-33 min were observed on ionosonde sounding virtual heights.

Goals of the present contribution.   Various experimental studies of the 11 August 1999 solar eclipse (cf. e.g., **?, ?, ?, ?, ?**) analyzed the relations between acoustic gravity wave generation mechanisms in Ionosphere and solar eclipse events. The present contribution aims at enlarging the scope of previously existing studies and at bringing new information about horizontal and vertical propagation characteristics. To do so, acoustic gravity waves detected during three different solar eclipses (11 August 1999, 3 October 2005 and 29 March 2006) are studied and compared. Description of these eclipses and corresponding data are detailed in Section **??** and Table **??**.

Elaborating on tools proposed in **?, ?** and **?**, this contribution also develops a wavelet transform based methodology to detect wave packets (or structures) propagating at Ionospheric heights and to measure, from data, their time, period and height locations, their wave vectors, phase and packet velocities. Techniques based on Fourier transforms were previously proposed. However, by definition, Fourier transforms are averaging, and hence mixing information, along time. Therefore, wave parameters measured at a given frequency can potentially result from the contribution of different waves sharing the same characteristic frequency but existing at different time positions, hence producing poor or inaccurate characterization of the waves. Wavelet decompositions, thanks to their being joint time and frequency representations, enable to disentangle the contribution of different structures whose time or frequency supports partially overlap. Therefore, they enable to better identify and analyze wave structures, to more accurately decide whether they consists of acoustic gravity waves or not and finally to better measure their corresponding propagation parameters.

Further developing this wavelet based approach, we inject measurements into the equations governing acoustic gravity wave propagation and, making use of an upper Atmosphere model (**?**), we fully characterize the propagating parameters of the detected structures. Acoustic gravity wave theory and the upper Atmosphere model are described in Section **??**. Wavelet decomposition

3

Event	First contact	Fourth contact	Maximum	Magnitude
11 Aug 1999	09:22	12:04	10:42	0.952
3 Oct 2005	08:01	10:32	09:15	0.539
29 Mar 2006	09:46	11:50	10:48	0.486

Table 1
Parameters of the solar eclipse events. parameters as observed above Průhonice ionospheric station, (According to NASA database, time is given in UT).

and wave packet detection and characterization are detailed in Section **??**. In Section **??** we will discuss the results and conclude.

2   Solar Eclipses and Data

Solar eclipse events.   In the present contribution, we analyze three different solar eclipse events. Two of them, 11 August 1999 and 29 March 2006, represent total solar eclipses, while the third one, 3 October 2005, is an annular solar eclipse. All three solar eclipse events occurred during periods of low geomagnetic activity. Indeed, as shown in Fig. **??**, Kp indices remained below or equal a maximum value of 3 (out of 9) for several consecutive days, indicating that Ionosphere remained in a quiet state. Therefore, we can consider that measurements reflect the variability due to the occurrence of the solar eclipses. The supersonic motion of the totality/ annularity footprint causes shock wave structures in Atmosphere, that are further reflected in ionospheric plasma. The parameters describing each solar eclipse are given in the Table **??**, as observed from Průhonice ionospheric station.

Data Measurements and time series.   In upper Atmosphere, acoustic gravity waves are observed directly as fluctuations of neutral gas or oscillations of the ionospheric plasma due to the coupling between the neutral and ionized components. Our measurements consists of vertical profiles of electron concentration. For the three eclipses, measurements were performed at the European mid-latitude ionospheric station Průhonice (Czech Republic; 49.9N, 14.6E), using vertical ionospheric sounding techniques. The 1999 solar eclipse was monitored using a classical ionosonde IPS 42 Kel Aerospace and data were collected with a 1-minute sampling period. This ionosonde was later (January 2004) replaced by the Digital Portable Sounder 4 (DPS4) hence used for the two latest solar eclipse events. For DPS4 measurements, lower resolution regimes were chosen to enable simultaneous record of ionograms and plasma drift. Hence data were collected with 2-minute and 3-minute sampling periods for the 2005 and 2006 events, respectively.

Real height vertical electron density profiles were derived from ionograms using two inversion techniques POLynomial ANalysis (**?**) and NHPC (**?**). Finally, from the real height electron density profiles, we obtain variations of the electron concentration X, as a function of time t, at fixed heights z:

$$X(t, z), \ t \in [T_m, T_M], z \in \mathbb{Z}. \tag{1}$$

where T_m and T_M denote the beginning and end of the measurement in UT. The spatial sampling period is 5km, corresponding to heights $\mathbb{Z} = \{155, 160, 165, \ldots, 255\}$ (in km). The time series for the three eclipses are shown in Fig. **??**, left column. The acoustic gravity wave detection procedures described below are performed on these $X(t, z)$ time series.

3   Acoustic gravity wave theory

acoustic gravity Wave propagation   At periods of minutes and larger, buoyancy effects become important due to atmospheric stratification and Atmosphere becomes dispersive and anisotropic. In such a medium, phase and energy no longer propagate along the same direction. Under an energy conservation assumption, the propagation of acoustic gravity waves is driven by the following ideal dispersion relation:

$$\omega^4 - \omega^2 \omega_a^2 - k_x^2 C^2 (\omega^2 - \omega_g^2) - C^2 \omega^2 k_z^2 = 0, \tag{2}$$

where k_x and k_z stand for the horizontal and vertical components of the wave vector, C for the speed of sound, ω_a for the angular acoustic cut-off frequency and ω_g for the angular buoyancy (or Brunt-Väisälä) frequency. This dispersion relation accounts for a nonlinear and dispersive propagation. It indicates the existence of two propagation frequency ranges: acoustic modes, with characteristic frequencies larger than the acoustic cut-off ω_a, gravity modes, with characteristic frequencies smaller than the Brunt-Väisälä ω_g. An important property of the gravity mode consists of that fact that energy flows up when phase travels down and vice versa, while for acoustic mode both energy and phase propagate jointly, either upward or downward. The phase propagation angle Φ (measured from the vertical, clock-wise) indicates the phase velocity (or wave vector) direction while the energy propagation angle γ (measured from the wave vector direction, clock-wise) indicates the packet velocity direction:

$$\tan \Phi = k_x / k_z, \tag{3}$$

$$\tan \gamma = \left(\left(\frac{\omega_a}{\omega} \right)^2 \sin \Phi \cos \Phi \right) / \left(1 - \left(\frac{\omega_a}{\omega} \right)^2 \sin^2 \Phi \right) \tag{4}$$

The modulus of the wave vector, the phase velocity and the vertical and horizontal components of the packet velocity are defined as:

$$k = k_x^2 + k_z^2, \tag{5}$$

$$v_\phi = \frac{\omega}{k}, \tag{6}$$

$$v_{p,x} = \left(C^2 k_x(\omega^2 - \omega_g^2)\right) / \left(\omega(2\omega^2 - \omega_a^2 - C^2 k^2)\right), \tag{7}$$

$$v_{p,z} = \left(C^2 k_z \omega^2\right) / \left(\omega(2\omega^2 - \omega_a^2 - C^2 k^2)\right). \tag{8}$$

Eqs. (**??**) to (**??**) are derived in e.g., **?** or **?**.

Neutral Atmosphere parameters. For a practical use of Eqs. (**??**) to (**??**), it is necessary to set the values of ω_a, ω_g and C that reflect the properties of the background neutral Atmosphere. In our analysis, we consider that the upper Atmosphere is well described by the Australian Standard Atmosphere model 2000 ($UASA2000$). The $UASA2000$ model is based on U.S. Standard Atmosphere, 1976 ($USSA1976$), and has been modified in the upper Atmosphere, above 86km (**?**). The $UASA2000$ model provides the scale height and acceleration due to gravity that are necessary to compute the speed of sound. The ratio between the specific heats at constant pressure and constant volume is a key factor in adiabatic processes and in determining the speed of sound in a gas. This ratio takes the value $\gamma = 1.66$ for an ideal mono-atomic gas and $\gamma = 1.4$ for a diatomic gas. Because Earth Atmosphere is predominantly a diatomic gas, we use this latter approximation (**?**, **?**).

4 Acoustic gravity wave detection and modeling

4.1 Wavelet Transform

• **Wave packet description and Fourier decomposition.** The goal is to extract wave propagation information from the data $X(z,t)$ sampled in time and space. In the literature, this has been addressed by performing a wave packet expansion of the data by means of Fourier Transform:

$$X(z,t) = \int_{\omega_0(z)-\Delta\omega}^{\omega_0(z)+\Delta\omega} X_0(\omega, z) \exp \imath(\omega t-)\ d\omega, \tag{9}$$

where $X_0(\omega, z)$ denotes the amplitude of the wave, obtained as the Fourier transform of $X(z,t)$ with respect to the time variable t, $\omega_0(z)$ and $\Delta\omega$ stand respectively for the central frequency and characteristic frequency width of the wave packet at altitude z. A methodology originally introduced in **??**, proposed to derive some of the Acoustic gravity wave parameters such as the characteristic frequency, the z- components of the wave vector and of the phase and packet velocities by tracking the evolution of extrema in amplitude and phase of $X_0(\omega, z)$ along z.

Elaborating on **?**, we extend this original idea to the wavelet framework. By replacing the Fourier transform with the wavelet transform, we obtain a description of the data $T_X(\omega, t, z)$ both along time and frequency. As detailed in Section **??**, a joint time and frequency representation enables more accurate detections and analyzes of wave structures.

• **Wavelet Transform.** Let $\psi_0(t)$ denote an elementary pattern, referred to as the mother-wavelet. It is required to have fast decreases both in the time and frequency domains, and to be a band-pass filter (i.e., to have zero mean):

$$\int_{\mathbb{R}} \psi_0(u)du, \equiv 0. \tag{10}$$

One defines a family of analyzing functions as translated and dilated templates of the mother-wavelet:

$$\psi_{a,t}(u) = \frac{1}{\sqrt{a}}\psi_0\left(\frac{u-t}{a}\right), \quad a > 0, \ z \in \mathbb{Z}. \tag{11}$$

The coefficients of the continuous wavelet transform are obtained by comparisons, by means of inner product, of the data $X(t, z)$ against the $\psi_{a,t}$:

$$T_X(a, t, z) = \int_{\mathbb{R}} X(u, z)\psi_{a,t}(u)du. \tag{12}$$

Because wavelets are band-pass filters, we can relabel, with a little abuse of notation, the wavelet coefficients $T_X(a, t, z) \equiv T_X(\omega, t, z)$ using the usual scale-frequency conversion: $\omega = \omega_\psi/a$, where ω_ψ is the central pulsation of the chosen mother-wavelet, defined as

$$\omega_\psi = 2\pi \frac{\int_0^{+\infty} \nu|\Psi_0(\nu)|^2 d\nu}{\int_0^{+\infty} |\Psi_0(\nu)|^2 d\nu}, \tag{13}$$

Ψ_0 standing for the Fourier transform of ψ_0.

Because we choose to use complex mother-wavelet, the wavelet coefficients $T_X(\omega, t, z)$ are complex numbers. Let $\{|T_X(\omega, t, z)|, \phi(\omega, t, z)\}$ denote their modulus and phase. Scalograms (also called wavelet power spectra) consist of the plots of $|T_X(\omega, t, z))|$ as a function of time t and period $P = 2\pi/\omega = 2\pi a/\omega_\phi$. Therefore, the scalograms $|T_X(\omega, t, z))|$ can be given the meaning of energy content of X, at height z, around time position t and around frequency $\omega = \omega_\psi/a$. Examples of scalograms obtained on electron concentration data are shown in Figs. **??** and **??**.

In the present work, we make use of Morlet and Paul (complex) mother-wavelets, defined as:

$$\text{Morlet} : \psi_{0,\mu}(t) = (\pi\sigma^2)^{-\frac{1}{4}} \exp(-\frac{t^2}{2\sigma^2}) \exp(\imath 2\pi\nu_0 t), \ \mu = 2\pi\sigma\nu_0, \tag{14}$$

$$\text{Paul} : \psi_{0,\mu}(t) = \frac{2^N \imath^N N!}{\pi(2N)!}(1 - \imath t)^{-(N+1)}, \qquad \mu = N, \tag{15}$$

where μ provides a degree of freedom that can be easily tuned to a given purpose. For instance, in the present work, it enables us to select the size of the time support of the mother wavelet. For these two chosen mother-wavelets, we have numerically computed ω_ψ from Eq. (**??**) above.

For a thorough introduction to wavelet transforms, the reader is referred e.g., to Mallat (1998). In the present work, we adapted the wavelet decomposition Matlab toolbox provided by Torrence and Compo (cf. **?**) to our purposes (Morlet wavelets with parameters $\mu = 6$ and 4 and Paul wavelets with parameters $\mu = 4$ and 2, were used).

4.2 Structure detection

The structure detection scheme we propose is organized in three key major steps:

(1) Data preprocessing and wavelet decomposition,
(2) Energy concentration detection at each altitude and maxima line tracking along altitude,
(3) Wave parameter measurements.

They are detailed below. For explanation purposes, the behavior of the entire detection/characterization/modeling procedure will be illustrated on a specific example structure, (corresponding to a superb gravity wave) occurring during the August, 11th, 1999 eclipse (GW1, in Table **??**). The corresponding data are shown in Fig. **??**(a).

• **Data preprocessing and wavelet decomposition.** For each altitude z independently, a high-pass filter is applied to the time series $\{X(t, z), t \in [T_m, T_M]\}_{z \in \mathbb{Z}}$ to suppress periods larger than 90min and focus on short term oscillations. Detrended time series are shown Fig. **??**(b). Then, complex wavelet coefficients are computed on these detrended data according to Eq. (**??**). Examples of scalograms are presented in Fig. **??**.

• **Wave packet detection.** First, for each scalogram $|T_X(\omega, t, z))|$ independently, local energy maxima are detected and their time position, period, amplitude and phase recorded. Second, local maxima that exist *jointly* over a *continuous range* of heights z, within a *same time-period neighborhood* are connected together to form *maxima lines*. When different maxima exist in a same time-period neighborhood, the chaining operation is conducted to favor smooth evolutions along z of the local maxima parameters. Each of these maxima lines correspond to the detection of a wave packet (or wave structure),

8

and consists of the following collection of information:

(1) Altitude range $z \in [\underline{z}, \overline{z}]$ within which the structure is detected;
(2) Precise time position $t_0(z)$ and pulsation $\omega_0(z)$ of the occurrence of the maximum at each height z and the corresponding amplitude $X_0(z) = X(t_0(z), z)$;
(3) Modulus $|T_X(\omega, t, z))|$ and phase $\phi(\omega, t, z)$ of the wavelet coefficients in the time-period neighborhood around the maxima position.

Scalograms, corresponding to different altitudes, showing local maxima marked with ('●') are displayed in Fig. **??**(a),(c) and (e). The practitioner can make use of a set of tools for visual inspection of the scalograms and for the manual selection of the structure (or maxima line) he wants to analyze. Then, he can zoom in the scalograms around the time and period locations of the chosen structure. This is illustrated in Fig. **??**(b),(d) and (f) for the same altitude. The selected structure is marked by the use of a '●'.

● **Wave packet characterisation.**   From the information collected for each wave packet, we derive the following collection of attributes.

(1) Mean time and pulsation defined as:
$$\underline{t_0} = \langle t_0(z) \rangle_z, \quad \underline{\omega_0} = \langle \omega_0(z) \rangle_z, \qquad (16)$$
where $\langle \cdot \rangle_z$ means that average is taken over the range of altitude $z \in [\underline{z}, \overline{z}]$.
(2) Components of the Wave vector, phase and packet velocities are measured as:
$$\left. \begin{array}{ll} k_z(\omega, t, z) = \partial\phi(\omega, t, z)/\partial z, & k_{0,z}(z) = \langle\langle k(\omega, t, z) \rangle\rangle_{t_0(z),\omega_0(z)}, \\ v_\phi^{(z)}(\omega, t, z) = \omega/k_z(\omega, t, z), & v_{\phi,0}^{(z)}(z) = \langle\langle v_\phi^{(z)}(\omega, t, z) \rangle\rangle_{t_0(z),\omega_0(z)}, \\ v_{p,z}(\omega, t, z) = \partial\omega/\partial k_z(\omega, t, z), & v_{p,0,z}(z) = \langle\langle v_{p,z}(\omega, t, z) \rangle\rangle_{t_0(z),\omega_0(z)}, \end{array} \right\} \quad (17)$$
where $\langle\langle \cdot \rangle\rangle_{t_0(z),\omega_0(z)}$ denote that we take the median within a narrow time-pulsation neighborhood centered around $t_0(z)$ and $\omega_0(z)$.

Fig. **??** shows $t_0(z)$, $P_0(z) = 2\pi/\omega_0(z)$, $k_{0,z}(z)$, $X_0(z)$, $v_{\phi,0}^{(z)}(z)$ and $v_{p,0,z}(z)$ measured according to the procedure described above for the chosen example structure.

This theoretically simple procedure calls for two important practical comments.
Comment 1   Computing the quantities above involves derivation. This is performed using a third-order or fifth-order finite difference procedure, depending on the range of heights available in the structure and border effects

9

are taken care of. Note that the computation of $v_{p,z}(\omega, t, z)$ requires a double derivation and is actually computed as the inverse of $\partial/\partial\omega(\partial\phi(\omega, t, z)/\partial z)$. This is numerically poorly conditioned and may lead to inaccurate results. This is further discussed in Section **??** where an acoustic wave is analyzed.

Comment 2 From ionospheric vertical sounding measurements, one only has access to vertical profiles of electron density and hence to the vertical components of the wave vector, phase and packet velocities. Therefore, in Eq. (**??**) above k_z and $v_{p,z}$ stand for the vertical components of the corresponding vectors. For the phase velocity, the situation is even more involved. In **???**, $v_\phi^{(z)}$ has been incorrectly associated to the z component of the phase velocity $v_{\phi,z}$. However, $v_\phi = \omega/k = \omega/k_z \cdot k_z/k = v_\phi^{(z)} cos\Phi$, while $v_{\phi,z} = v_\phi cos\Phi$, hence, $v_{\phi,z} = v_\phi^{(z)} cos^2\Phi$. When the phase propagation direction is close to the vertical direction, the error is negligible, this is however not the case for close to horizontal phase propagation.

4.3 Structure modeling

No further information can be extracted from the data themselves. To decide whether a detected wave packet corresponds or not to the propagation of an acoustic gravity wave, it can be compared to the theoretical acoustic gravity wave propagation model recalled in Section **??**, making use of the upper Atmosphere model.

First, from the Atmosphere model, we derive the values of $\omega_a(z), \omega_g(z)$ and $C(z)$, for all $z \in [\underline{z}, \overline{z}]$. Comparing the measured $w_0(z)$ to $\omega_a(z)$ and $\omega_g(z)$ enables to check whether the detected structure packet consists of a gravity or acoustic waves.

Second, for all $z \in [\underline{z}, \overline{z}]$ and all t and ω in the time-period neighborhood associated to the studied structure, we derive $k_x(\omega, t, z)$ from the dispersion relation in Eq. (**??**) by plugging-in the measured $k_z(\omega, t, z)$ and the calculated $\omega_a(z), \omega_g(z)$ and $C(z)$.

Third, making use of Eqs. (**??**) to (**??**), we derive the phase and energy propagation angles $\Phi(\omega, t, z)$ and $\alpha(\omega, t, z) = \Phi(\omega, t, z) + \gamma(\omega, t, z)$, respectively, measured clockwise from the vertical direction. Then, we compute the wave vector $k(\omega, t, z)$ and the phase velocity $v_\phi(\omega, t, z)$ from Eqs. (**??**) to (**??**). Combining previous results yields the phase velocity components $v_{\phi,z}(\omega, t, z) = v_\phi(\omega, t, z) \cos \Phi(\omega, t, z), v_{\phi,z}(\omega, t, z) = v_\phi(\omega, t, z) \sin \Phi(\omega, t, z)$. To finish with, Eqs. (**??**) to (**??**) provide the packet velocity components $v_{p,x}(\omega, t, z)$ and $v_{p,z}(\omega, t, z)$. Fourth, from these quantities, we compute the median $\langle\langle\cdot\rangle\rangle_{t_0(z),\omega_0(z)}$ (as defined in Section **??** above) for each quantity hence

obtaining

$$
\left.
\begin{aligned}
\text{Wave Vector} \quad k_{0,x}(z) &= \langle\langle k_x(\omega, t, x)\rangle\rangle_{t_0(z),\omega_0(z)}, \\
k_0(z) &= \langle\langle \sqrt{k_x(\omega, t, x)^2 + k_z(\omega, t, z)^2}\rangle\rangle_{t_0(z),\omega_0(z)}, \\
\text{Wavelength} \quad \lambda_0(z) &= 2\pi/k_0(z), \\
\text{Phase Angle} \quad \Phi_0(z) &= \langle\langle \Phi(\omega, t, z)\rangle\rangle_{t_0(z),\omega_0(z)}, \\
\text{Energy Angle} \quad \alpha_0(z) &= \langle\langle \alpha(\omega, t, z)\rangle\rangle_{t_0(z),\omega_0(z)}, \\
\text{Phase velocity} \quad v_{\phi,0}(z) &= \langle\langle v_\phi(\omega, t, z)\rangle\rangle_{t_0(z),\omega_0(z)}, \\
v_{\phi,0,z}(z) &= \langle\langle v_{\phi,z}(\omega, t, z)\rangle\rangle_{t_0(z),\omega_0(z)}, \\
v_{\phi,0,x}(z) &= \langle\langle v_{\phi,x}(\omega, t, z)\rangle\rangle_{t_0(z),\omega_0(z)}, \\
\text{Packet velocity} \quad v_{p,0,z}(z) &= \langle\langle v_{p,z}(\omega, t, z)\rangle\rangle_{t_0(z),\omega_0(z)}, \\
v_{p,0,x}(z) &= \langle\langle v_{p,z}(\omega, t, x)\rangle\rangle_{t_0(z),\omega_0(z)}, \\
v_{p,0}(z) &= \langle\langle \sqrt{v_{p,x}(\omega, t, z)^2 + v_{p,z}(\omega, t, z)^2}\rangle\rangle_{t_0(z),\omega_0(z)},
\end{aligned}
\right\} \tag{18}
$$

Fig. **??** shows, for the chosen example structure, the quantities computed according to the procedure described above. Also, it compares the computed $v_{\phi,0,z}(z)/cos^2\Phi_0(z)$ with the measured $v_{\phi,0}^{(z)}$ as well as the computed and measured z-component of the packet velocities.

Both for detection and modeling, the central point of our procedures consists of the fact that all quantities are computed for each triplet (ω, t, z) independently and that a local median is performed *a posteriori* over a narrow time-pulsation neighborhood. Moreover, it is a remarkable fact that all the calculations related to the wave modeling require the use of a single quantity measured from data: $k_z(\omega, t, z) = \partial\phi(\omega, t, z)/\partial z$.

4.4   Wavelet based acoustic-gravity wave detection and modeling toolbox

All procedures and programs used to detect and characterize acoustic gravity wave were written and implemented in MATLAB, by ourselves. A graphical user interface of this toolbox is implemented for a friendly use and allow easy selection of the structures. This toolbox is available upon request.

5 Results and discussions

5.1 Wave activity

The three solar eclipses are characterized by an increase of the wave-like oscillation in the acoustic-gravity period range during and after the event. This finding is in agreement with other experimental studies **?**, **?**, **?** related to observation of the August 11, 1999 event. However, the amplitudes of the oscillations do not remain at the same level during the whole solar eclipse event. Fig. **??**(b) shows much larger amplitudes of the fluctuation during the initial phase compared to those occurring after the maximum solar disk occultation. Figs. **??**(d) and **??**(f) indicate completely different situations: Larger electron concentration oscillation amplitudes are observed after the eclipse maximum and remain present after the fourth contact. Moreover, the two most recent eclipses are characterized by significantly lower magnitudes compared to that of the first one. The decrease of the solar radiation flux is proportional to the magnitude of the eclipse and is reflected in the depletion of the electron concentrations at all ionospheric heights (compare Fig. **??**, left column, plot (a) against (c) and (e)).

After removal of these global trends, the residual oscillations are analyzed using the wave detection procedures described above. This reveals that numerous wave-packets are detected propagating within the ionospheric plasma, before, during and after the solar eclipse events. Most observed waves are characterized by periods ranging from 20 minutes to 70 minutes and all of them but one consist of gravity waves. All the detected and analyzed waves are listed in Table **??**. They are sorted according to their occurrence time (with respect to the phases of the solar eclipse event). Within data we detected also several waves before the solar eclipse events. These waves we do not report in the paper since they are very probably not related to the solar eclipse. Due to the fact that all three events occur during morning hours and because the performed measurements cover also sunrise hours, such waves can have their origin the Solar Terminator movement. Therefore, waves appearing before first contact of each eclipse event are not presented and further discussed.

5.2 Gravity waves

Let us analyze in details three of the detected waves that occur as first propagating structures within the studied height range.

11 August 1999: Gravity wave 1. This is the wave chosen to illustrate

Event	name	Period	Occurrence	Propagation
11 August 1999	GW1	15 min, 30 min	Initial	upward/downward
	AW1	3-4 min	Initial	upward/downward
	GW2	22 min	After	upward
3 October 2005	GW1	43min	Maximum	upward
	GW2	20min	Recovery	upward
	GW3	65min	After	upward
	GW4	30min	After	upward
	GW5	32min	After	upward
	GW6	22min	After	upward
29 March 2006	GW1	30min	Initial	upward
	GW2	40min	After	upward

Table 2

Detected waves. List of the detected and analyzed waves with occurrence period and time (with respect to the eclipse phase). Period of the wave denotes dominant period of the structure.

the behaviors of the detection and modeling procedures described in Section ?? and in Fig. ??. It was obtained with Paul wavelet ($\mu = 4$). Shortly after the first contact around 9h 20min UT, an upward propagating structure with period about 30 minutes and a downward traveling wave with period about 15 minutes are found. Both of them have a source region located at height 200km. Fig. ?? reports the measurements obtained from the data characterizing these waves. One notices that the downward wave slightly precedes the upward wave (Fig. ?? (a)) and that the maximum amplitude of the upward wave is located around 240km (see Fig. ?? (c)). An important property of gravity waves lies in the fact that the phase propagates downward while the wave is moving upward or vice versa. Fig. ?? shows the wavevectors and the vertical components of the phase and packet velocities measured from the data. The positive sign of the packet velocity together with the negative sign of the phase velocity confirm that a gravity wave is found, that propagates upward from altitude 200km. Conversely, the gravity wave propagates downward below 200km. Fig. ?? shows all the wave parameters - wave vector, wavelength, phase and packet velocities, phase and energy angles - characterizing the propagations and derived from acoustic gravity wave theory. The validation for the detection of a gravity wave is highlighted by the difference between energy (α) and phase (Φ) angle which is around 90 degrees. Moreover one notices that these waves propagates along directions close to the diagonals. Characteristic wavelength is found to be around 200 km.

In this case, as in most cases, we find an extremely satisfactory agreement

between the $z-$ components of the phase and packet velocities measured from the data and derived from the model. This agreement takes into account **Comment 1**, made in Section **??** regarding the discrepancy between the measured quantity v_ϕ^z and the $z-$ component of the phase velocity $v_{\phi,z}$. These agreements provide us with clear indications confirming the validity of the detection of a gravity wave and a clear validation of the relevance of our combination of measurements made from data and modeling obtained from equations.

3 October 2005: Gravity wave 1. For the 3 October 2005 event, the first detected wave structure occurs at 9h 12min, close to the eclipse maximum (see Fig. **??**(a)), computed using Paul wavelet ($\mu = 6$). This gravity wave with period about 43 minutes (Fig. **??**(b)) propagates upward between 155 km and 200 km (as seen from the positive packet velocity and negative phase velocities (cf. Fig. **??**(e) and (f))). Wave amplitude maximum appears to be at height 180 km. Fig. **??** illustrates the complete propagation characteristics of the gravity wave. Its wavelength is found to be around 200 km (Fig. **??**(d)).

29 March 2006: Gravity wave 1. For the 29 March 2006, inspection of the wavelet power spectrum (computed using Paul wavelet ($\mu = 6$), cf. Fig. **??**(a)) indicates that a well developed structure is observed 14 minutes only after the first contact. This structure propagates through the lower part of the analyzed ionospheric region, from 160 km up to 205 km, with a period around 30 minutes (Fig. **??**(b)). It reaches its maximum amplitude at height around 190 km (Fig. **??**(c)). Fig. **??**(d) shows the vertical component of the wave vector. The values of the $z-$ components of the phase (negative) and packet (positive) velocities obtained from the data indicate that we observe an upward propagating gravity wave (cf. Fig. **??**(e) and (f)). The complete set of propagation parameters is illustrated in Fig. **??**(a)-(f). Fig. **??**(b) shows an excellent agreement between estimated and modeled vertical components of the phase velocity. The measured and modeled vertical packet velocities do not match perfectly in the whole range (for reasons discussed in Section **??**), however, there is a reasonable agreement with respect to sign and magnitude.

Discussion. Equivalent analyses and plots for each of the detected structures mentioned in Table **??** are available upon request or can be found at `http://www.ufa.cas.cz/html/climaero/sauli.html`. The study of these structures yields the following comments.
The gravity wave activity increases after a notably larger delay for the annular solar eclipse compared to the total solar eclipses: waves are found during maximum phase only for the former while they occur during the initial phase for the latter. This difference in gravity waves generation/occurrence can likely be explained by differences in the terrestrial atmosphere cooling: the border

between sunlit and eclipsed region is much sharper in the case of total eclipse. Analyzing wave propagations, we observe predominantly upward propagating structures. The wave structure that propagate upward and downward from the source region located around 200 km height consists of an exceptional case related to the solar eclipse of August 11, 1999. Such a situation does not repeat in any of the two other analyzed events, when the coverage of the solar disk is much lower. This finding might reflect that for the two later events, we mostly observe signatures of the shock wave.

For all the detected gravity waves, the values of the energy propagation angles α (Fig. **??**, **??** (f) and Fig. **??** (f)) indicate an oblique propagation direction. The difference between energy (α) and phase (Φ) angles, close to 90 degrees, confirm the gravity wave nature of the detected waves.

The wave characterisation procedures developed here enable us to discriminate between the waves occurring before the solar eclipses, for instance waves produced by the Solar Terminators at sunrise (**?,?**), and those induced by the solar eclipse.

5.3 Acoustic wave

During the initial phase of the August, 11, 1999 event, we found a line of maxima existing over a large range of heights z and with a period ranging from 3 to 4 minutes (cf. Fig. **??**). The identical signs of packet and phase velocities (cf. Fig. **??**), together with the propagation period range suggest that this is an acoustic wave. Fig. **??** shows the characteristics of the wave as derived from the model. For this wave, while the agreement between the measured and derived $z-$components of the phase velocity is very satisfactory, this is not the case for the packet velocity (cf. Fig. **??**(e) and (f)). This can be easily understood as the measured packet velocity involves taking an empirical double derivative, at periods ($3-4$ minutes) which are extremely close to the sampling period (1 min): this is hence a ill-conditioned numerical operation. This points out a major difficulty in detecting and characterizing acoustic waves: detecting waves, whose periods are of the order of a few minutes, from data collected at sampling rates commonly used, above 1 min, is barely possible and even meaningless ; a relevant tracking of acoustic waves requires the use of sampling periods well below the minute. However, in the 1999 event, the combined use of a wavelet-based time-frequency representation, together with the exceptionally low 1-min sampling period, enables us to unambiguously detect an acoustic wave, which, as far as we know, has very rarely been achieved. Moreover, the use of the equation-based modeling that we proposed here allows us to accurately identify its propagating parameters. For instance, we find that the energy and phase angles are close one from the other as opposed to what is found for gravity waves. For this wave, we also find that the value of the energy angle indicate an oblique propagation of the wave. Hence, despite this

15

sampling rate issue, the modeling of the acoustic wave proposed proves valid and gives satisfactory results.

6   Conclusions

In the present contribution, we showed that, taking advantage of the excellent joint time and frequency localization properties of the wavelet transform, we are able to detect and characterize wave structures. The detection relies on the identification of a collection of local modulus maxima, occurring simultaneously through a continuous range of heights. From the (derivation) of the phase of the complex wavelet coefficients, we managed to measure the $z-$ components of the wave, phase and packet velocity vectors. Furthermore, making use of the acoustic gravity wave propagation equations, we managed to fully characterize the corresponding propagating parameters. This modeling part only relies on the use of the measured $z-$component of the wave vector. A key point in our approach lies in the use of sequences of vertical profiles of electron concentration and in the derivation of vertical and horizontal characteristics of the propagating pulse. Making use of this tools, we were able to identify numerous gravity waves and one acoustic wave. Hence, our analysis confirms the occurrence and production of acoustic gravity waves, at ionospheric heights, during solar eclipses. Notably, we observed that for strong amplitude total eclipses AGW occur extremely quickly after the beginning of the event. Also, we highlighted the difficulties in acoustic wave detection and modeling as well as the need for much higher sampling rate when acoustic waves are targeted. We believe that the use of the toolbox proposed here brings significant improvements and benefits with respect to efficient wave detections and can hence be easily used by the ionospheric community.
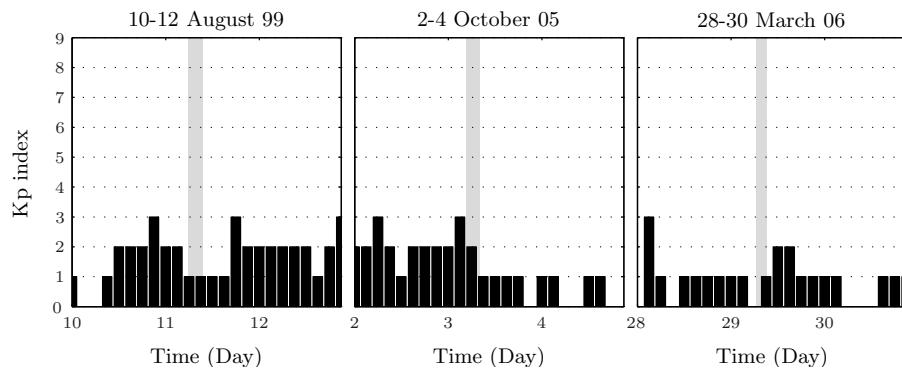
Fig. 1. **3-hour Kp index.** Geomagnetic activity during three solar eclipses events. The grey shaded areas indicate occurrences time of the eclipses.
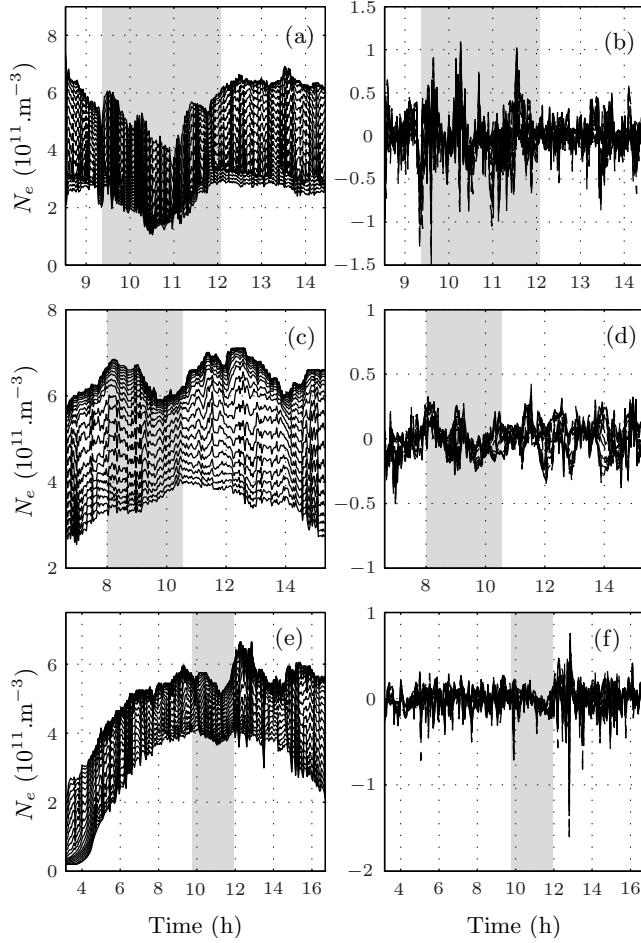
Fig. 2. **Electron concentrations.** Variations of the electron concentrations (at fixed heights 155 km - 255 km) as a function of time for eclipse 1999, 11 August (a) and (b); 2005, 3 October (c) and (d); and 2006, 29 March (e) and (f), (left column) and the corresponding fluctuations left after removing the main trend (right column). The grey shaded areas indicate occurrences time of the eclipses.
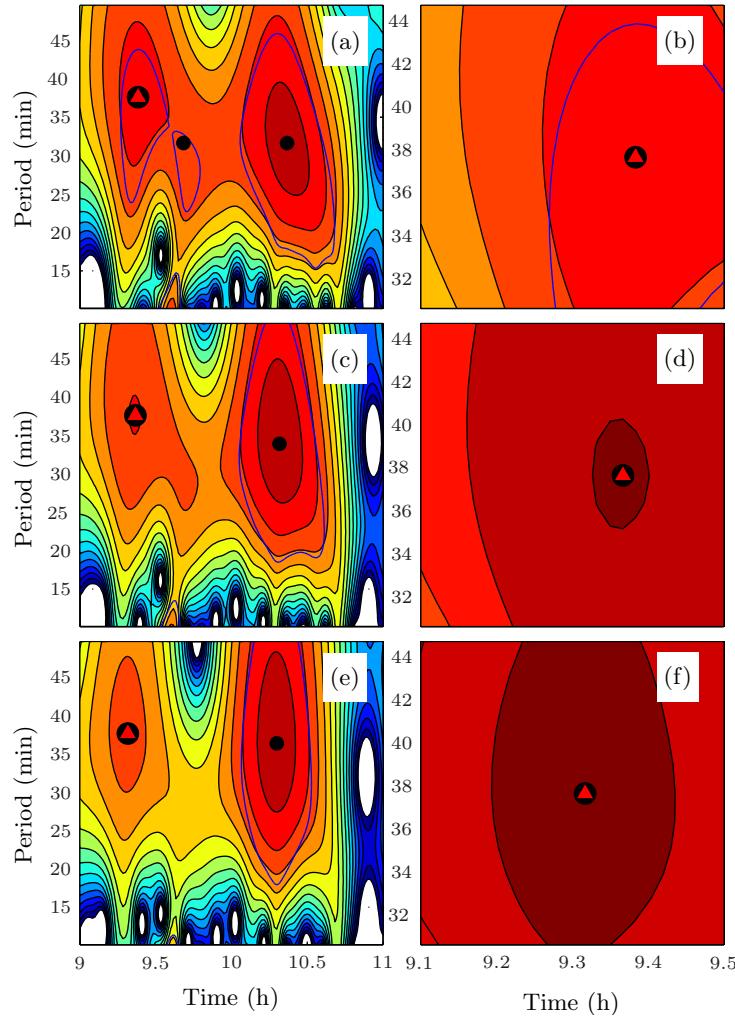
Fig. 3. **Scalograms, 11 August 1999.** Examples of three scalogram plots at three consecutive heights 220km (a) and (b); 215 km (c) and (d); and 210 km (e) and (f). In left column, the time range is selected to cover the initial solar eclipse phase. Local maxima line are marked with "●". Around 9h15min UT, there exists a well developed line of local maxima, marked with a "▲", that coincide in time and period over a significant range of heights z. Panels (b), (d) and (f) represent the focus on this maxima in the period range 31-45 minutes between 9h UT and 9h30min UT. Paul wavelet, $\mu = 4$.
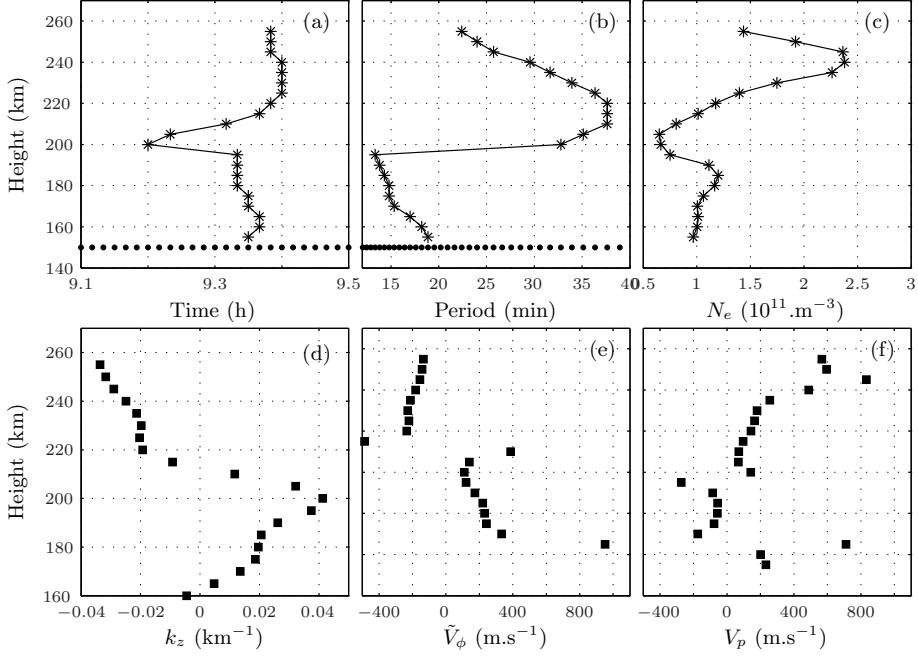
Fig. 4. **11 August 1999,GW1: Detection.** Time location (a), period (b) and amplitude (c) of the detected wave, with the vertical components of the wave vector k_z (d), phase velocity $v_\phi^{(z)}$ (e) and packet velocity $v_{(p,z)}$ (f). Paul wavelet, $\mu = 4$.
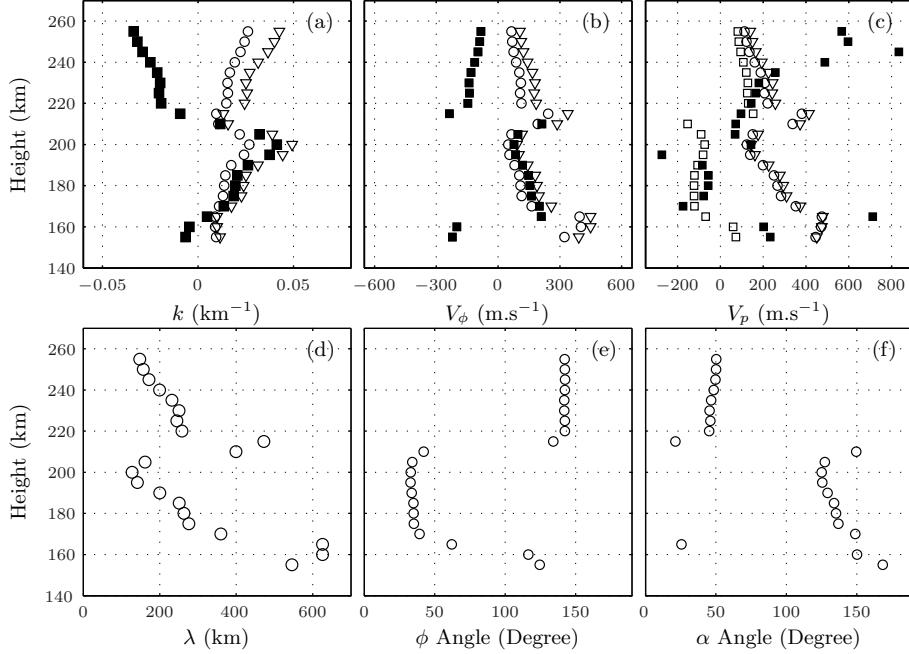
Fig. 5. **11 August 1999,GW1: Modeling.** Wave parameters computed from the AGW theory: Wavevector (a), Phase velocity (b), packet velocity (c), wave number (d), energy (e) and phase (f) angles. For the vectors of first row, the '□' correspond to the measured (black) and computed (white) $z-$components, the '○' correspond to the horizontal components while the '▽' are related to the modulus. Paul wavelet, $\mu = 4$.

20
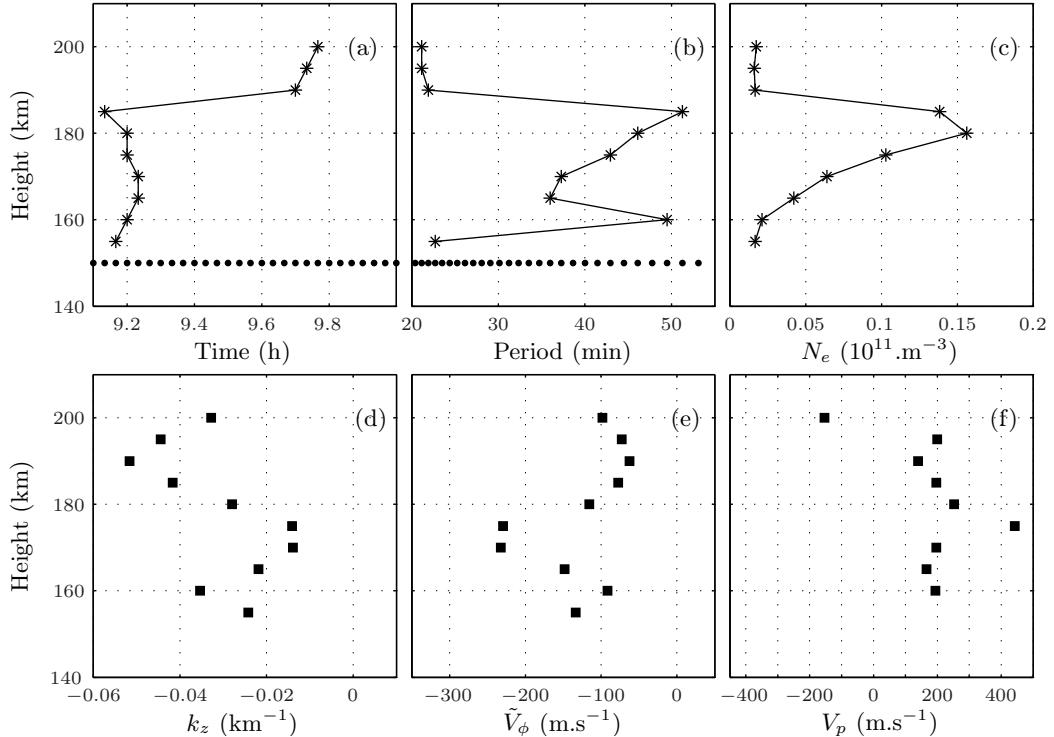
Fig. 6. **3 October 2005, GW1: Detection.** Same legend as Fig. **??**. Paul wavelet, $\mu = 6$.
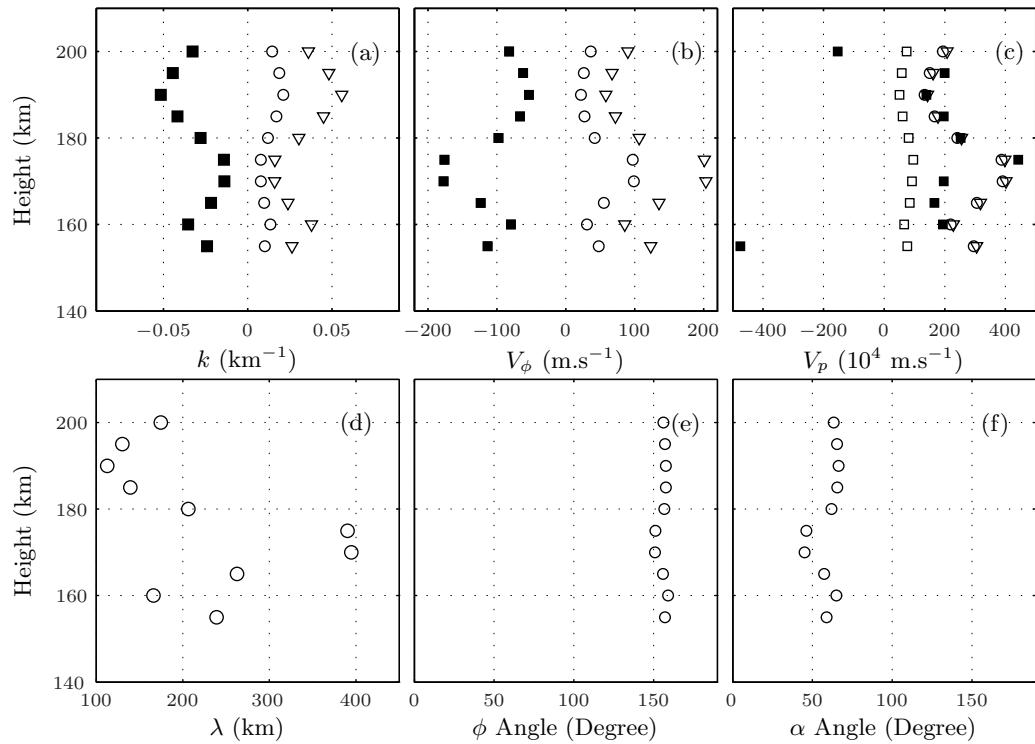
Fig. 7. **3 October 2005, GW1: Modeling.** Same legend as Fig. **??**. Paul wavelet, $\mu = 6$.
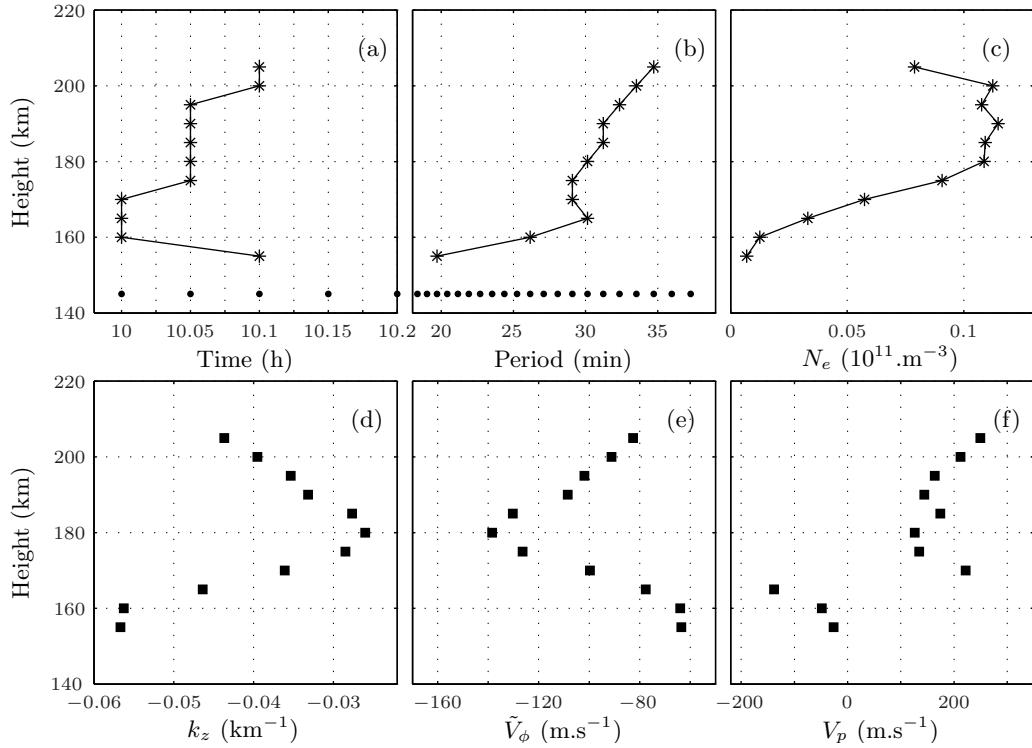
Fig. 8. **29 March 2006, GW1: Detection.** Same legend as Fig. **??**. Paul wavelet, $\mu = 6$.
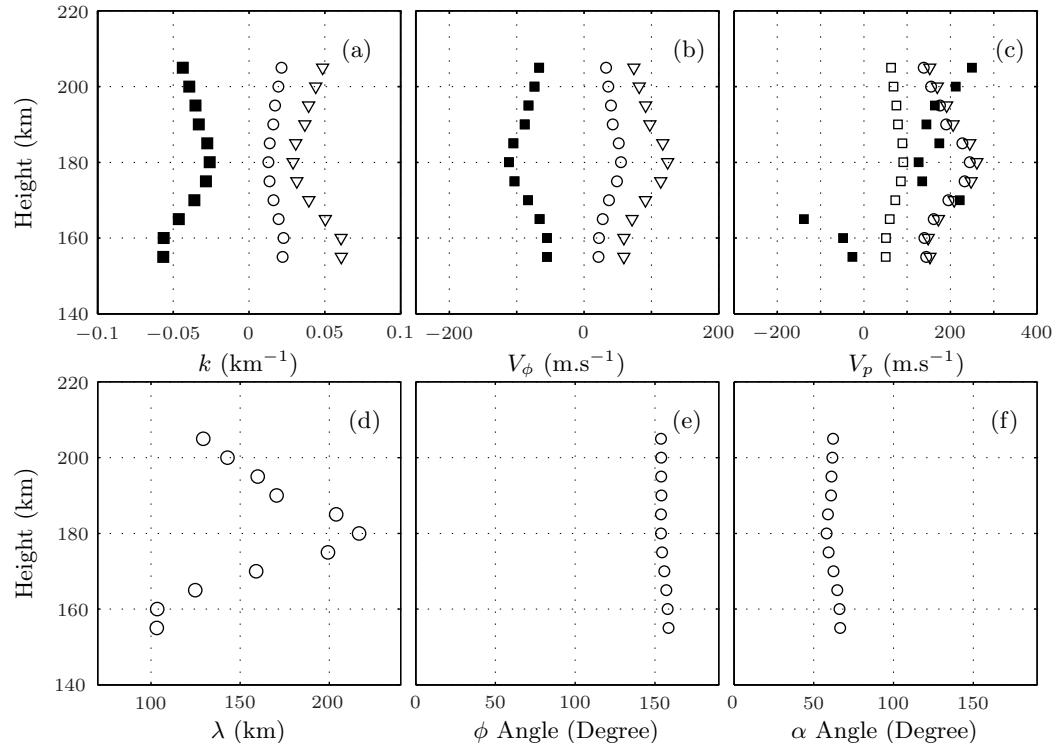
Fig. 9. **29 March 2006, GW1: Modeling.** Same legend as Fig. **??**. Paul wavelet, $\mu = 6$.
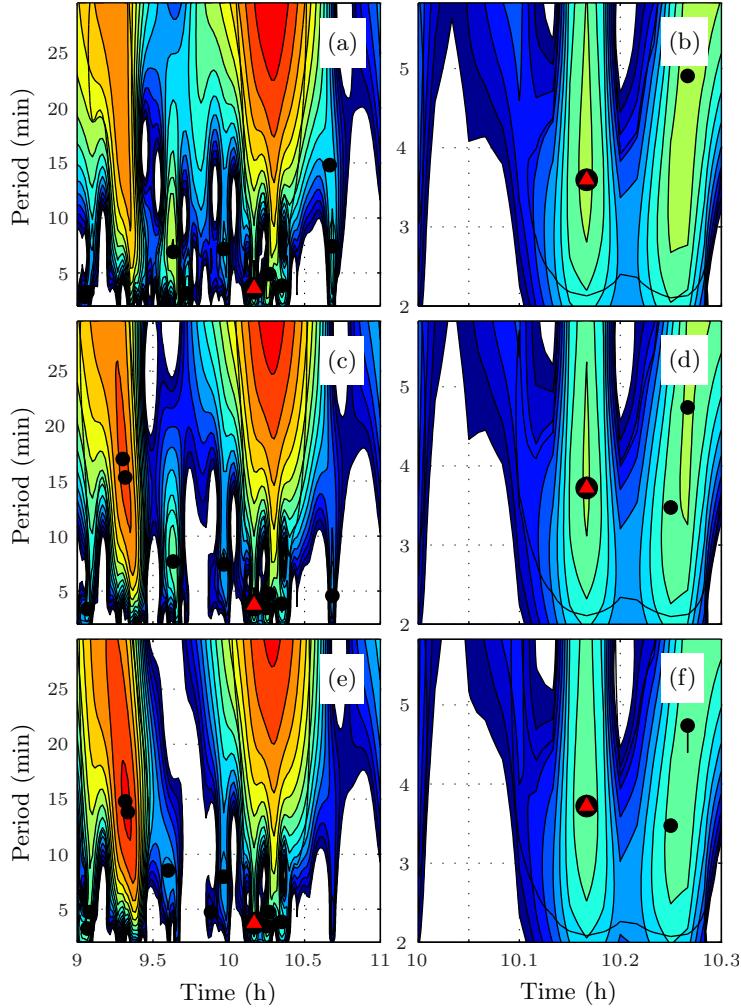
Fig. 10. **Scalograms, 11 August 1999.** Examples of three scalogram plots at three consecutive heights 200km (a) and (b); 195 km (c) and (d); and 190 km (e) and (f). In left column, the time range is selected to cover the initial solar eclipse phase. Local maxima line are marked with "●".. Between 10h UT and 10h20min UT, there is well developed local maxima ,marked with a "▲", that coincides in time and period over a significant range of heights zs. Panels (b), (d) and (f) represent the focus on this maxima in the acoustic mode period range 2-6 minutes around 10H15min UT.
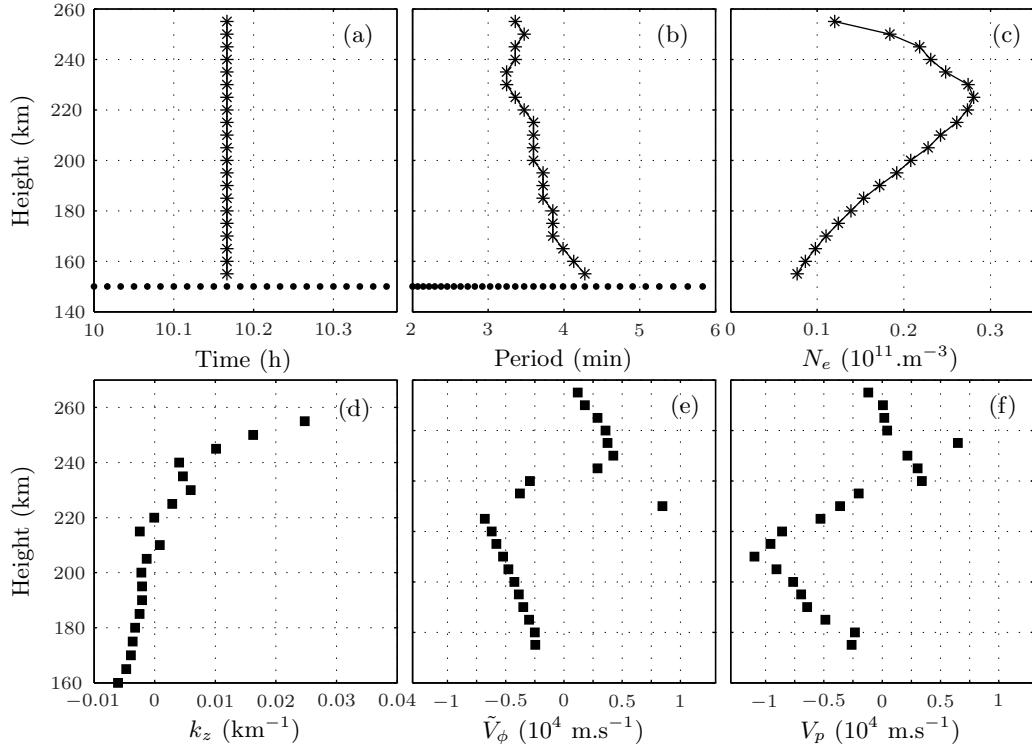
Fig. 11. **11 August 1999,AW1: Detection.** Same legend as Fig. **??**. Paul wavelet, $\mu = 2$
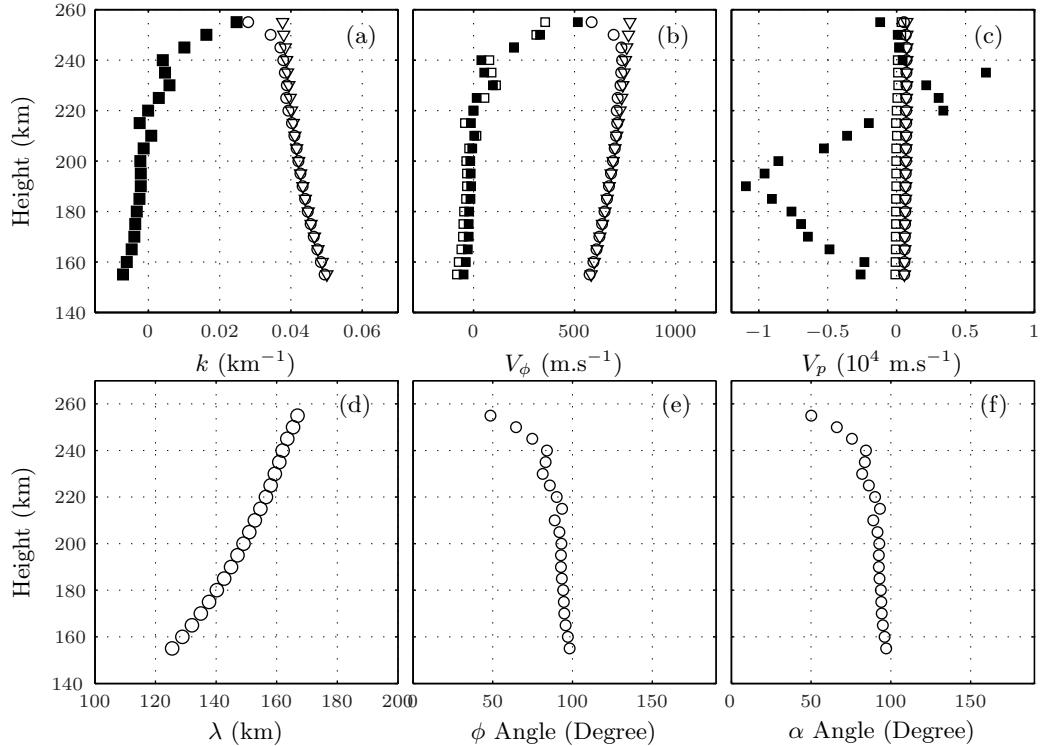

Fig. 12. **11 August 1999,AW1: Detection.** Same legend as Fig. **??**. Paul wavelet, $\mu = 2$

References

Altadill, D., Sole, J.G., Apostolov, E.M., 2001a. Vertical structure of a gravity wave like oscillation in the ionosphere generated by the solar eclipse of August 11, 1999. Journal of Geophysical Research - Space Physics, 106 (A10), 21419-21428.

Altadill, D., Gauthier, F., Vila, P., Sole, J.G., Miro, G., Berranger, R., 2001b. The 11.8.1999 solar eclipse and the ionosphere: a search for distant bow-wave. Journal of Atmospheric and Solar-Terrestrial Physics, 63 (9), 925-930.

Chimonas, G., Hines, C.O., 1970. Atmospheric Gravity Waves Induced by a Solar Eclipse. Journal of Geophysical Research, 75, 4, 875-875.

Davies, K., 1990. Ionospheric Radio. Peter Peregrinus Ltd, London, UK.

Farges, T., Le Pichon, A., Blanc, E., Perez, S., Alcoverro, B., 2003 Response of the lower atmosphere and the ionosphere to the eclipse of August 11, 1999. Journal of Atmospheric and Solar-Terrestrial Physics, 65, (6), 717-726.

Feltens J., Jakowski N., Noll C., 2001. High-Rate SolarMax IGS/GPS Campaign "HIRAC/SolarMax". CDDIS Bulletin, 16 (3).

Fritts, D.C., Vadas, S.L., Wan, K., Werne, J.A., 2006. Mean and variable forcing of the middle atmosphere by gravity waves. Journal of Atmospheric and Solar-Terrestrial Physics, 68, 247-265.

Fritts, D.C., Alexander, M.J., 2003. Gravity dynamics and effects in the middle atmosphere. Reviews of Geophysics 41.

Fritts, D.C., Luo, Z., 1993. Gravity Wave Forcing in the Middle Atmosphere Due to Reduced Ozone Heating During a Solar Eclipse. Journal of Geophysical Research, 98, 3011-3021.

Fritts, D.C., 1989. A review of gravity wave saturation processes, effects, and variability in the middle atmosphere. Pure and Applied Geophysics 130, 343Ű371.

Galushko, V.G., Paznukhov, V.V., Yampolski, Y.M., Foster, J.C, 1998. Incoherent scatter radar observations of AGW/TID events generated by the solar terminator. Annales Geophysics 16, 821-827.

Harkrider, D.G., 1964. Theoretical + Observed acoustic gravity Waves from Explosive Sources in Atmosphere Journal of Geophysical Research, 69 (240, 5295- .

Hines, C.O., 1960. Internal atmospheric gravity waves at ionospheric heights. Canadian Journal of Physics, 38, 1441-1481.

Hooke, W.H., 1968. Ionospheric irregularities produced by internal atmospheric gravity waves. Journal of Atmospheric and Solar-Terrestrial Physics, 30, 795-823.

Hocke, K., Schlegel, K., 1996. A review of atmospheric gravity waves and traveling ionospheric disturbances: 1982Ű1995. Annales Geophysicae, 14, 917.

Huang, X., Reinish, B.W, 1996. Vertical electron density profiles from the digisonde network. Advances in Space Research, 18(6), 121-129.

Laštovicka, J., 2006. Forcing of the ionosphere by waves from below. Journal

of Atmospheric and Solar-Terrestrial Physics, 68, 479-497.

Liu J.Y., Hsiao, C.C., Tsai, L.C., Liu, C.H., Kuo, F.S., Lue, H.Y., Huang, C.M., 1998. Vertical Phase and Group velocities of internal gravity waves derived from ionograms during the solar eclipe of 24 october1995. Journal of Atmospheric and Solar-Terrestrial Physics, 60, 1679-1686.

Mallat, S., 1998. A Wavelet Tour of Signal Processing. Academic Press, San Diego.

Muller-Wodarg I.C.F, Aylward, A.D., Lockwood, M., 1998. Effects of a Mid-Latitude Solar Eclipse on the Thermosphere and Ionosphere - A modeling Study. Geophysical Reseach Letters, 25 (20), 3787-3790.

http://sunearth.gsfc.nasa.gov/eclipse/eclipse.html

Pietrobon, S.S., 2000. Unofficial Australian Standard Atmosphere 2000. http://www.sworld.com.au/steven/space/atmosphere/

Pröls, G.W., 2004. Physics of the Earth's Space Environment. An Introduction. Springer-Verlag, Berlin, Germany.

Rishbeth H., Moffett, R.J., Bailey, G.J., 1969. Continuity of Air Motion in the Mid-latitude Thermosphere. Journal of Atmospheric and Solar-Terrestrial Physics, 31, 1035-1047.

Row, R.V., 1967 acoustic gravity Waves in Upper Atmosphere Due to a Nuclear and an Earthquake. Journal of Geophysical Research, 72 (5): 1599- .

Šauli, P., Abry, P., Boška, J., Duchayne, L., 2006a. Wavelet Characterisation of Ionospheric Acoustic and Gravity Waves occuring during the Solar Eclipse of August 11, 1999. Journal of Atmospheric and Solar-Terrestrial Physics, 68, 586-598.

Šauli, P., Abry, P., Altadill, D., Boška, J., 2006b. Detection of the wave-like structures in the F-region electron density: two station measurements. Sudia Geophysica and Geodetica, 50, 131-146.

Somsikov, V.M., 1991. Waves in the atmosphere excited by the Solar Terminator. Geomagnetism and Aeronomy, 31, 1. (in russian)

Titheridge, J.E., 1985. Ionogram analysis with the generalised program POLAN. UAG report-93.

Torrence, C., Compo, G.P., 1998. A Practical Guide to Wavelet Analysis. Bulletin of American Meteorological Society, 79, 1, 61-78.

United States Committee on Extension to the Standard Atmosphere, 1976. U.S. Standard Atmosphere 1976. Atmospheric Administration, National Oceanic and National Aeronautics and Space Administration, United States Air Force, Washington D.C.

Walker, G.O., Li, T.Y.Y., Wong, Y.W., Kikuchi, T., Huang, Y.N., 1991. Ionospheric and Geomagnetic Effects of the Solar Eclipse of 18 March 1988 in East-Asia. Journal of Atmospheric and Solar-Terrestrial Physics, 53 (1-2), 25-37.